# JACS

Article

High-Rate Intercalation without Nanostructuring in Metastable Nb$_2$O$_5$ Bronze Phases

Kent J. Griffith, Alexander C. Forse, John M. Griffin, and Clare P. Grey*

Department of Chemistry, University of Cambridge, Cambridge CB2 1EW, U.K.

S Supporting Information

ABSTRACT: Nanostructuring and nanosizing have been widely employed to increase the rate capability in a variety of energy storage materials. While nanoprocessing is required for many materials, we show here that both the capacity and rate performance of low-temperature bronze-phase TT- and T-polymorphs of Nb$_2$O$_5$ are inherent properties of the bulk crystal structure. Their unique "room-and-pillar" NbO$_6$/NbO$_7$ framework structure provides a stable host for lithium intercalation; bond valence sum mapping exposes the degenerate diffusion pathways in the sites (rooms) surrounding the oxygen pillars of this complex structure. Electrochemical analysis of thick films of micrometer-sized, insulating niobia particles indicates that the capacity of the T-phase, measured over a fixed potential window, is limited only by the Ohmic drop up to at least 60C (12.1 A·g^{-1}), while the higher temperature (Wadsley−Roth, crystallographic shear structure) H-phase shows high intercalation capacity (>200 mA·h·g^{-1}) but only at moderate rates. High-resolution $^{6/7}$Li solid-state nuclear magnetic resonance (NMR) spectroscopy of T-Nb$_2$O$_5$ revealed two distinct spin reservoirs, a small initial rigid population and a majority-component mobile distribution of lithium. Variable-temperature NMR showed lithium dynamics for the majority lithium characterized by very low activation energies of 58(2)−98(1) meV. The fast rate, high density, good gravimetric capacity, excellent capacity retention, and safety features of bulk, insulating Nb$_2$O$_5$ synthesized in a single step at relatively low temperatures suggest that this material not only is structurally and electronically exceptional but merits consideration for a range of further applications. In addition, the realization of high rate performance without nanostructuring in a complex insulating oxide expands the field for battery material exploration beyond conventional strategies and structural motifs.
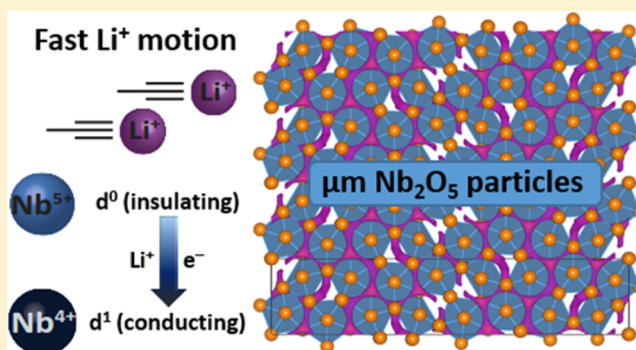
INTRODUCTION

There is a growing need for high-power, high-capacity energy storage materials for applications that require faster rate performance than traditional battery materials can offer, along with higher charge storage capability than can be achieved with supercapacitor systems. Unless nanosized, conversion materials and two-phase intercalation compounds commonly used in lithium-ion batteries generally do not deliver high power due to the kinetics associated with major structural transformations. Electric double-layer capacitors (EDLCs) can deliver high rate performance but are limited to relatively low volumetric and areal energy densities as redox reactions offer the opportunity for 10−100 times greater charge storage than the electrostatic mechanism of EDLCs.[1,2] In lithium-ion batteries, realization of the maximum capacity of an electrode material in a given potential window is inherently dependent upon the ability of lithium to reach the particle interior. This has generally limited high rate performance to materials with short diffusion distances typically achieved via nanoscaling or nanostructuring of the particles.

The disadvantages of the synthesis and use of nanoparticles and nanoarchitectures for battery applications are well known:

high surface area leading to increased dissolution and increased surface−electrolyte interface (SEI) formation, low packing density, toxicity, high cost, chemical waste generation, scalability issues, and often many-step synthetic complexity.[3−5] Preparation of energy-dense materials with high capacity and good rate performance through a simple and efficient synthetic route is clearly desirable but evidence from, e.g., Li$_4$Ti$_5$O$_{12}$, LiFePO$_4$, and TiO$_2$ suggests that this is not generally observed.

Niobium(V) oxides, in the potential window from ca. +2.0 to +1.0 V vs Li$^+$/Li, have shown impressive rate and capacity as intercalation electrodes. In this voltage range, safety and stability issues from SEI formation associated with electrolyte instability below +1.0 V vs Li$^+$/Li, as well as lithium dendrite formation, can be avoided.[6−8] Furthermore, as lithium does not alloy with aluminum until 300 mV vs Li$^+$/Li,[9] copper foil can be substituted with significantly cheaper and lighter aluminum foil as the anode current collector. The phase stability of Nb$_2$O$_5$ is complex and at ambient temperature and pressure many metastable polymorphs exist that depend on heating con-
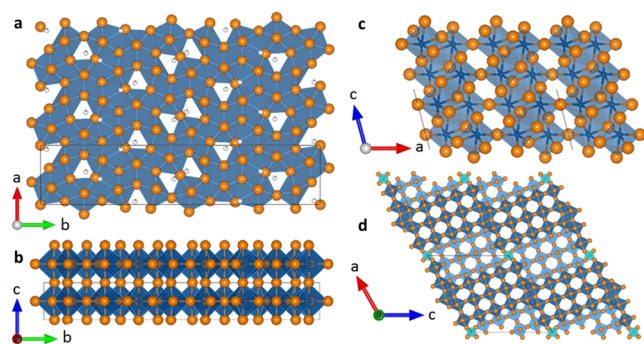
Figure 1. Crystal structures of (a,b) T-Nb_2O_5, (c) B-Nb_2O_5, and (d) H-Nb_2O_5. Oxygen and (partially occupied) niobium sites are represented by orange and (partially filled) blue spheres, respectively.

ditions, precursors, and synthesis procedures.[10] In this study, we examine four polymorphs: TT-Nb_2O_5,[11−13] T-Nb_2O_5 (*Pbam*, Figure 1a,b),[14] B-Nb_2O_5 (*C2/c*, Figure 1c),[15] and H-Nb_2O_5 (*P2/m*, Figure 1d).[16] Regarding nomenclature, the T designation comes from the German *tief*, which means low, as in low temperature; the B polymorph was named for its crystal habit (*blätter* or bladed); and the H designates high as it is the high-temperature phase.[10] T-Nb_2O_5 is structurally similar to the tungsten bronzes but composed of primarily highly distorted octahedral and pentagonal bipyramidal Nb environments rather than regular octahedra. Partially occupied niobium sites (totaling 0.8 of the 16.8 niobium atoms per $Nb_{16.8}O_{42}$ unit cell) with high coordination and long Nb−O interatomic distances are proposed in the crystal structure to balance the charge from 42 oxygen atoms per unit cell.[14] The TT-phase is a metastable structure whose structural details are not fully understood but are apparently similar to those of T-Nb_2O_5.[11] On the basis of diffraction data, TT-Nb_2O_5 has been described as a disordered modification of T-Nb_2O_5, the disorder being related to modulation of niobium atoms above and below the mirror plane at (*x*, *y*, 0.5) in T-Nb_2O_5.[11] Monoclinic B-Nb_2O_5 possesses a TiO_2(B)-like structure. H-Nb_2O_5, another monoclinic polymorph and the phase which is not known to convert to any other polymorph as a function of temperature, fits into the Wadsley−Roth family of crystallographic shear structures with $(3×4)_1$ and $(3×5)_∞$ ReO_3-like blocks of octahedra. Shared octahedral edges along shear planes at the periphery of the blocks account for the oxygen:metal ratio of 2.5. The blocks are infinite parallel to *b*, and the subscripts 1 and ∞ denote block connectivity in the *ac* plane.[17]

Recent studies on the TT- and T-polymorphs have shown excellent rate and cycle life performance on a variety of nanoscaled and nanostructured morphologies. Examples include nanobelts,[18] nanofibers,[19] nanosheets,[20,21] nanoparticles/nanocrystals, templated mesoporous nanoparticles,[22−27] nanocrystalline Nb_2O_5/carbon nanotube nanocomposites,[28] nanocrystalline Nb_2O_5/graphene nanocomposites,[29,30] nanocrystalline Nb_2O_5/carbide-derived carbon nanocomposites,[31] and Nb_2O_5@carbon core−shell nanocrystals.[32] While some electrochemical and structural aspects of bulk TT-, T-, and H-Nb_2O_5, prepared from solid-state methods, have been investigated,[33,34] their rate behavior has evidently not been characterized. In this work, we examine the electrochemical properties of a family of Nb_2O_5 polymorphs synthesized via oxidation of niobium(IV) oxide. This simple solid-state route enables access to the low-temperature metastable phases and has been used to produce TT-, T-, B-, and H-Nb_2O_5

previously;[10] however, few details were given in the earlier study and, to the best of our knowledge, (i) no systematic synthetic procedure has been reported; (ii) no electrochemistry of Nb_2O_5 phases from NbO_2 has been reported; and (iii) the electrochemistry of B-Nb_2O_5, irrespective of precursor, has not been previously discussed. Along with the ease of synthesis relative to nanostructuring, solid-state methods produce larger particles with decreased contributions from electric double-layer capacitance, surface and near-surface phenomena, and non-bulk-like local atomic structure environments, facilitating a study of the inherent properties of Nb_2O_5. Lithium environments and dynamics from $^{6/7}$Li solid-state NMR and bond valence sum maps performed as part of this study aid the understanding of the structural origin of the anomalous electrochemical performance in micrometer-sized metal oxides. These tools show degenerate diffusion pathways with a very low activation energy for Li motion on the order of a few k_BT (ca. 60−100 meV). Through this investigation, we find that the accessible capacity and rate performance of the low-temperature Nb_2O_5 polymorphs is a general feature of the structure type and not a function of nanoscaling or nanostructuring.

■ EXPERIMENTAL METHODS

Synthesis. Nb_2O_5 polymorphs were synthesized by heating separate aliquots of NbO_2 (Alfa Aesar, 99.5+%) in alumina crucibles in air for 24 h at 19 temperature points between 200 and 1100 °C spaced at 50 °C increments. The samples were heated at a ramp rate of 10 °C·min^{-1} until the desired temperature was attained; the temperature was then held for 24 h before ambient cooling. Thermal gravimetric analysis (TGA) was performed on a Mettler Toledo TGA/SDTA 851 thermobalance. Samples were placed in a tared 100 μL alumina crucible and the mass was recorded from 50 to 1000 °C in steps of 1 °C·min^{-1} under constant air flow (50 mL·min^{-1}). A blank, with an empty crucible, was recorded under the same heating conditions and subtracted from the sample data. The data were numerically differentiated to obtain differential thermogravimetry (DTA) curves.

Electrochemistry. Cathodes (in half-cell configuration) were prepared by agate mortar and pestle grinding of Nb_2O_5, Super P carbon (Timcal), and Kynar polyvinylidene difluoride (PVDF, Arkema) in an 8:1:1 mass ratio with *N*-methyl-2-pyrrolidone (NMP, Sigma-Aldrich, 99.5%, anhydrous) to form a viscous slurry. High-carbon proof-of-concept electrodes were prepared in a similar manner but with an active material:carbon:binder ratio of 3:6:1. The slurry was tape cast onto an aluminum foil current collector with a 150−200 μm doctor blade. After drying for at least 12 h at 60 °C, 1 cm^2 circular cathodes were cut via a punch press. Unless otherwise noted, mass loadings were 4−6 mg Nb_2O_5·cm^{-2}. Coin cell batteries were constructed in an argon-filled glovebox with O_2 and H_2O levels <1 ppm. The electrolyte−solvent system consisted of 1 M $LiPF_6$ dissolved in a 1:1 volume ratio of ethylene carbonate/dimethyl carbonate (EC:DMC, Merck). The aforementioned cathode, a glass microfiber (Whatman) separator saturated with electrolyte−solvent, a lithium metal foil anode (Sigma-Aldrich, 99.9%) on a stainless steel current collector, and a wave spring were compressed within a standard 2032-type coin cell casing. All electrochemical measurements were performed with a Bio-Logic potentiostat/galvanostat instrument running EC-Lab software. In each coin cell, the niobium oxide/carbon/binder film served as the working electrode and the lithium metal as both the counter electrode and reference electrode. Discharge/charge took place within the range from +3.0 V to +1.2 V or +1.0 V with respect to Li$^+$/Li. Galvanostatic charge/discharge data were numerically differentiated to give differential voltage curves. Specific cycling conditions are denoted in the text for each experiment. For the preparation of samples for NMR analysis, thick (150−750 mg) pellets of pure Nb_2O_5 powder were cold pressed at 5 MPa and assembled into coin cells as above. These pellets were discharged at

$100-500 \ \mu A \cdot cm^{-2}$ until a desired degree of lithiation was reached. For clarity, in this Article, C rate refers to inverse hours required to reach the theoretical capacity of $201.7 \ mA \cdot h \cdot g_{Nb_2O_5}^{-1}$ (e.g., C/5 implies a current of $40.34 \ mA \cdot g_{Nb_2O_5}^{-1}$), and discharge refers to lithium insertion into the Nb_2O_5 structure. Theoretical capacity for a one-electron reduction from Nb^{5+} to Nb^{4+} is $201.7 \ mA \cdot h \cdot g^{-1}$ based on the mass of Nb_2O_5.

X-ray Diffraction (XRD). Laboratory powder X-ray diffraction (PXRD) patterns were recorded at room temperature on a Panalytical Empyrean diffractometer emitting Cu Kα (1.540598 Å + 1.544426 Å) radiation. Patterns were recorded from 5–80° 2θ in steps of 0.017° 2θ. Rietveld analysis was performed in GSAS[35] and GSAS-II[36] with the aid of the CMPR toolkit.[37] Crystal structures and isosurfaces (with bond valence energy level cutoff set to 2.0 eV, see Discussion) were visualized in VESTA 3.0.[38]

Morphological Analysis. Brunauer–Emmett–Teller (BET) surface areas were obtained from nitrogen adsorption isotherms at 77 K. BET data were collected on a TriStar 3000 gas adsorption analyzer (Micromeritics Instrument Corp., V6.08). Scanning electron microscopy (SEM) images were taken with a Σigma VP microscope (Zeiss). Tap density was recorded on an AutoTap (Quantachrome Instruments) instrument operating at 257 taps·min⁻¹. The tap densities were measured according to ASTM international standard B527-15, modified to accommodate a 10 cm³ graduated cylinder.

6/7Li Solid-State Nuclear Magnetic Resonance. One- and two-dimensional solid-state NMR experiments were performed in a 4.0 mm probehead on a 200 MHz Bruker Avance III spectrometer at the ^7Li Larmor frequency of 77.7 MHz and on a 700 MHz Bruker Avance III spectrometer at the ^6Li Larmor frequency of 103.0 MHz and ^7Li Larmor frequency of 272.0 MHz. Magic angle spinning (MAS) up to 14 kHz was applied; the specific rotational frequency is denoted for each experiment. One-dimensional spectra were recorded with a single $\pi/2$ pulse or Hahn-echo pulse sequence; the applied $\pi/2$ pulse lengths for ^6Li and ^7Li were 7.00 μs and 2.60–3.75 μs, respectively. Two-dimensional exchange spectroscopy (EXSY) measurements were performed with a rotor-synchronized $\pi/2-t_1-\pi/2-t_{mixing}-\pi/2-t_2$ pulse sequence, where t_{mixing} is a variable mixing period during which the nuclei are allowed to interact via chemical and/or spin diffusion. Spectra were collected as a function of temperature for 1D, 2D, spin–lattice (T_1), and spin–spin (T_2) relaxation measurements of selected samples. A saturation recovery pulse sequence was employed for T_1 measurements: a series of $\pi/2$ pulses was first applied to eliminate bulk magnetization (M_0) along z, and then the z-magnetization was allowed to relax during a recovery time (t) before recording the magnetization (M_t) over a range of recovery times. A variable-delay spin echo sequence was used to measure T_2. As the sample temperature cannot be measured directly with sufficient accuracy under MAS conditions, a temperature calibration was performed based on the temperature-dependent shift of ^{207}Pb in $Pb(NO_3)_2$[39] (Supporting Information, Figure S1). All samples were ground with an agate mortar and pestle and packed into 4.0 mm ZrO_2 rotors in an Ar-filled glovebox with <1 ppm of O_2 and <1 ppm of H_2O; lithiated samples were washed with dimethyl carbonate (3 × 3 mL) to remove any residual $LiPF_6$ and dried *in vacuo* before being ground and packed. The $^{6/7}Li$ spectra were referenced with a secondary reference ($^{6/7}Li$ 1:1 at./at.), Li_2CO_3, at +1.1 ppm versus the 1.0 M LiCl (aq) primary reference at 0.0 ppm.

■ RESULTS AND DISCUSSION

1. Structural Characterization of Nb₂O₅ Polymorphs.

Thermal gravimetric analysis of NbO_2 and Nb (Supporting Information, Figure S2) showed that the onset of oxidation for NbO_2 occurs at a temperature significantly below that for oxidation of Nb metal—290 °C versus 420 °C—allowing a greater range of metastable phases to be prepared with this starting material. A systematic X-ray diffraction investigation revealed that four from the range of polymorphs with a nominal composition of Nb_2O_5 were observed upon thermal oxidation
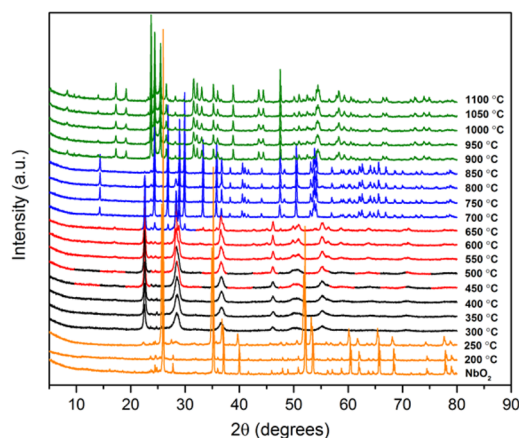

Figure 2. XRD patterns of phases observed upon heating NbO_2 in air. The patterns dominated by NbO_2, $TT-Nb_2O_5$, $T-Nb_2O_5$, $B-Nb_2O_5$, and $H-Nb_2O_5$ are shown in orange, black, red, blue, and green, respectively. Lines with more than one color indicate a temperature where a significant amount of more than one phase was present.

of NbO_2 (Figure 2). While some changes are apparent after 24 h at 250 °C, NbO_2 does not oxidize to Nb_2O_5 until ca. 300 °C in air, $TT-Nb_2O_5$ being the first oxidized phase that is observed. Three further irreversible phase transitions are observed at higher temperature: nearly phase-pure $T-Nb_2O_5$ is found from approximately 550 to 600 °C, $B-Nb_2O_5$ is observed from 700 to 850 °C, and $H-Nb_2O_5$ is observed at and above 900 °C. Rietveld analysis (Supporting Information, Figure S3) revealed minor impurities from the reactant or other polymorphs in all but the H-phase. A color change is observed from deep blue, d^1, niobium(IV) to white, d^0, niobium(V) for all samples heated above 400 °C. This is an indication that the oxidation is complete for the T-, B-, and H-phases. The TT-phase is a pale gray-blue and thus may retain a small (ca. <0.5%)[10] fraction of niobium(IV). The observed color changes are in accordance with the color change from white, through gray-blue, toward dark blue observed as lithium is inserted into any of the Nb_2O_5 structures in this study and elsewhere.[40]

Unlike the step changes in crystal structure from NbO_2 to orthorhombic and then through two distinct monoclinic Nb_2O_5 polymorphs, the surface and particle morphology, as viewed by SEM (Figure 3 and Supporting Information, Figure S4),
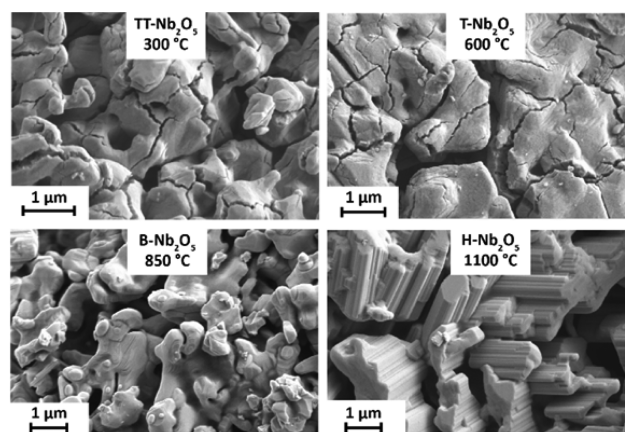

Figure 3. SEM images showing the particle sizes and morphologies of the Nb_2O_5 polymorphs obtained from oxidation of NbO_2; phase and synthesis temperature are denoted.

Table 1. Physical Properties of Micrometer-Sized Nb_2O_5: BET Surface Area, As Determined from N_2 Adsorption Isotherms at 77 K, and Tap Density of Four Polymorphs of Nb_2O_5 Synthesized from NbO_2 via Thermal Oxidation

phase	synthesis temperature (°C)	BET surface area ($m^2 \cdot g^{-1}$)	tap density ($g \cdot cm^{-3}$)
TT-Nb_2O_5	300	1.8 ± 0.1	1.4 ± 0.1
T-Nb_2O_5	600	1.9 ± 0.1	1.4 ± 0.1
B-Nb_2O_5	850	1.5 ± 0.1	1.2 ± 0.1
H-Nb_2O_5	1100	0.7 ± 0.1	1.8 ± 0.1
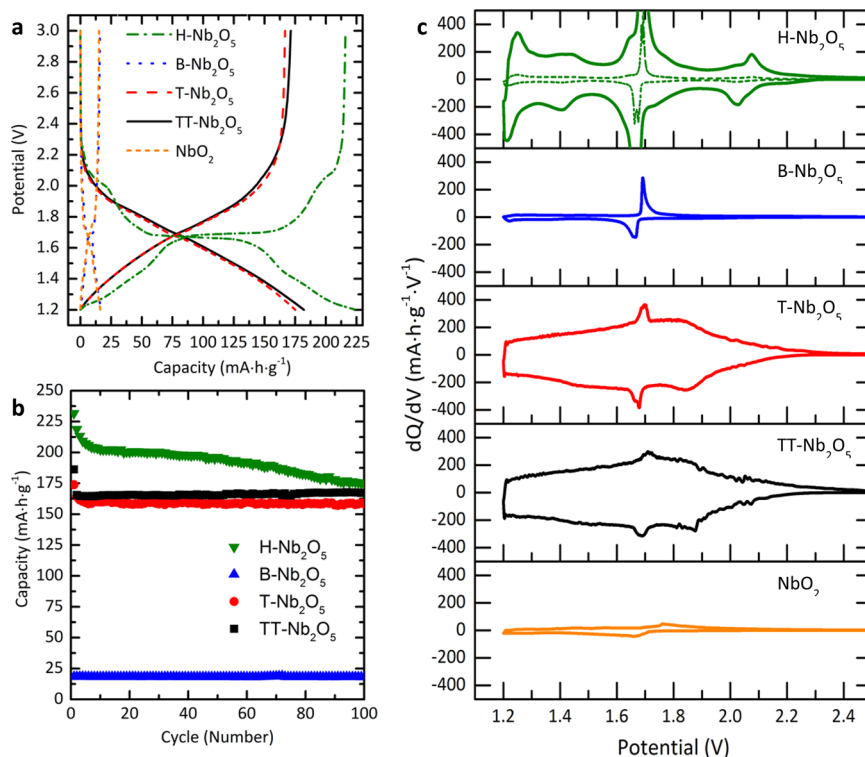
Figure 4. Galvanostatic discharge−charge curves for the Nb_2O_5 polymorphs from 3.0 to 1.2 V (a) Electrochemical discharge/charge profiles obtained at a rate corresponding to C/10. (b) Cycle tests at either 1C (T, TT) or C/10 discharge/charge with a constant voltage charge step (B, H). (c) Differential capacity plots derived from the discharge/charge profiles in (a); solid lines are on the same scale, while the dashed green line is shown at 1/20 scale to reveal the peak positions in H-Nb_2O_5.

transformed more smoothly upon heating. After treatment at 300 °C in the TT-phase, anhedral particles (i.e., without well-formed crystal faces) with cracked-mud-like topology dominated which, at 600 °C in the T-phase, had partially annealed. The samples heated to 850 °C yielded rounded steps on interconnected subhedral particles of the B-phase, which, after 1100 °C treatment crystallized further to capped euhedral particles of several micrometers with distinctly striated edges in the H-phase. In addition to the smaller primary particle features, a larger secondary particle size (more visible in Supporting Information, Figure S4) can be considered which corresponds to discrete particles composed of interconnected primary particles; this secondary particle size is of the order of tens of micrometers. BET surface area measurements revealed a quite small surface area, on the order of 1−2 $m^2 \cdot g^{-1}$, for all phases. For further particle characterization, tap density was measured and reported with BET surface area in Table 1. As volumetric, rather than gravimetric, energy density dictates many applications, the tap density of Nb_2O_5 from solid-state synthesis is noteworthy at 1.2−1.8 $g \cdot cm^{-3}$. By comparison, commercial TiO_2 nanopowders of 5−20 nm have almost an order of magnitude smaller tap density (0.12−0.24 $g \cdot cm^{-3}$).[41] Thus, the Nb_2O_5 phases examined in this study differ in

structure and morphology but all are μm-scale, dense, and extremely low surface area.

2. Electrochemical Properties of Nb_2O_5 Polymorphs. Electrochemical lithiation of NbO_2 and the four Nb_2O_5 polymorphs revealed a range of structure-driven mechanisms. Chronopotentiometric discharge and charge were performed at a rate of C/10 where kinetic limitations should be minor. The results (Figure 4a), demonstrate (i) a high intercalation capacity and three distinct regions for H-Nb_2O_5; (ii) a close-to-linear sloping voltage profile for T- and TT-Nb_2O_5; (iii) a very small capacity for B-Nb_2O_5 and NbO_2; and (iv) a low overpotential between charge and discharge for all phases in the electrochemical window 3.0 to 1.2 V vs Li^+/Li. Cycling studies (Figure 4b) were performed with galvanostatic discharge and charge at 1C for T- and TT-Nb_2O_5 and C/10 for B- and H-Nb_2O_5 with an additional constant voltage charge step (CCCV charging) at 3.0 V that is widely employed to optimize charging while preventing overcharge. H-Nb_2O_5 showed a first cycle capacity of 235 $mA \cdot h \cdot g^{-1}$ but dropped to 175 $mA \cdot h \cdot g^{-1}$ after 100 cycles. Conversely, B-Nb_2O_5 stored only 20 $mA \cdot h \cdot g^{-1}$ on first discharge but retained that capacity with no diminution over the recorded cycle range. After a first cycle loss of ∼25 $mA \cdot h \cdot g^{-1}$, TT- and T-Nb_2O_5 exhibited reversible capacities of

165 and 160 mA·h·g^{-1}, respectively, for 100 cycles with the capacity of the TT-phase edging slightly upward after the initial capacity loss. Differential capacity plots (Figure 4c) reveal the (de)lithiation behavior in more detail. H-Nb$_2$O$_5$ exhibits reversible peaks centered at 2.05, 1.67, 1.42, and 1.22 V with a significant amount of charge stored at intermediate potentials between the peaks. B-Nb$_2$O$_5$ and NbO$_2$ exhibit only one small peak at 1.68 and 1.71 V, respectively; however, the cathodic–anodic peak separation in NbO$_2$ is much greater, indicating a kinetic limitation even at C/10. To the best of our knowledge, bulk NbO$_2$ intercalation has not been reported but is evidently not significant between 3.0 and 1.2 V vs Li$^+$/Li. NbO$_2$ electrochemical behavior is unlike that seen for the 2H layered transition metal dichalcogenide phase LiNbO$_2$,[42] though both involve the Nb^{4+}/Nb^{3+} redox couple. In LiNbO$_2$ the reversible delithiation from LiNbO$_2$ to Li$_{0.5}$NbO$_2$ occurs from 2.5 to 3.0 V.[43] TT- and T-Nb$_2$O$_5$ store charge nearly evenly across the potential range 1.9−1.2 V with minor peaks at 1.68 V. Accounting for the minor quantity of B- and H-Nb$_2$O$_5$ present in the lower temperature phases, these small dQ/dV peaks may be related to one of the higher temperature polymorphs. Note that although the capacity of the TT- and T-phases in Figure 4 corresponds to ca. 0.8 Li per Nb, one full equivalent of lithium can be intercalated if the potential cutoff is moved below 1.0 V. The limit of 1.2 V was chosen because a lower cutoff voltage resulted in decreased cycle life at least in part due to SEI formation. The discharge profile features, cycle life, and capacity for TT-, T-, and H-Nb$_2$O$_5$ at low current density (slow rate) are in agreement with previous work from solid-state[33] and nanostructured[19,25,44] synthesis methods.

3. Charge Storage Kinetics of Micrometer-Sized Nb$_2$O$_5$.

Charge storage kinetics, i.e., rate dependences, are contingent upon a range of interrelated factors such as atomic structure, electronic structure, particle size, particle geometry, and intra- and interparticle porosity. Numerous studies have focused on the latter, microstructural, aspects of Nb$_2$O$_5$ by designing creative synthetic strategies to attain nanocrystals,[28,29] nanowires,[45] nanosheets,[20,21] and even hierarchical structures of nanoparticles containing nanoscale porosity.[22,46] To determine whether the high rate properties discussed in the literature for Nb$_2$O$_5$ are limited to nanoscale or nanostructured analogues, a rate performance study (Figure 5) was conducted on thick (4−6 mg·cm^{-2}) electrodes of the micrometer-sized Nb$_2$O$_5$ particles. Under these conditions, the capacity of H-
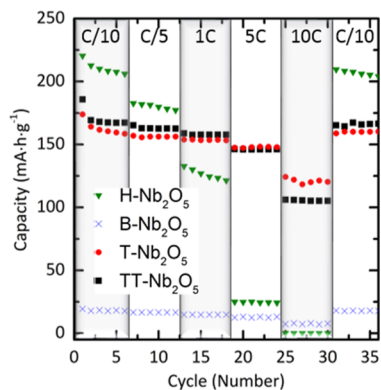
Figure 5. Relationship between discharge rate and capacity for thick films (4−6 mg·cm^{-2}) of bulk H-, B-, T-, and TT-Nb$_2$O$_5$ between 3.0 and 1.2 V vs Li$^+$/Li.

Nb$_2$O$_5$ is highly correlated with discharge rate; a change from C/10 to 1C causes a 50% decrease in capacity and no charge storage is observed beyond 10C. The capacity of B-Nb$_2$O$_5$ is only weakly rate dependent but a maximum value of 20 mA·h·g^{-1} means that only 10% of the niobium sites are reduced; this suggests that a surface or near-surface redox process is occurring and thus a weak structure−rate relationship might be expected. Significantly, T- and TT-Nb$_2$O$_5$ retain much of their initial capacity under fast discharge conditions: 150 mA·h·g^{-1} at 5C and 100−120 mA·h·g^{-1} at 10C (3.5 min discharge for a capacity of 120 mA·h·g^{-1}). A plot of discharge potential vs capacity as a function of current (Figure 6) for (a) T-Nb$_2$O$_5$
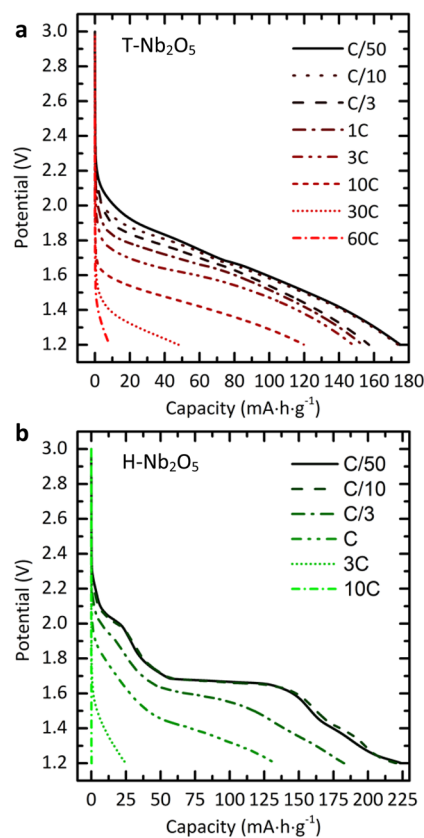
Figure 6. Discharge behavior of (a) T-Nb$_2$O$_5$ and (b) H-Nb$_2$O$_5$ over ca. 3 orders of magnitude of current density. After five cycles, cells were cycled between 3.0 and 1.2 V vs Li$^+$/Li at the rate shown. The charging step is rate limiting for T-Nb$_2$O$_5$; discharge was examined after CCCV charging so as to always examine the discharge behavior of the fully delithiated material.

and (b) H-Nb$_2$O$_5$ displays fundamental differences between the lithiation of these polymorphs. At the initial discharge current pulse, both phases show a potential drop down to the niobium redox potential with a superimposed IR drop associated with the total resistance from the electrode and cell components. From this stage, under a small current with a consequently small Ohmic contribution, T-Nb$_2$O$_5$ shows an approximately linear relationship between potential and charge while H-Nb$_2$O$_5$ contains distinct shoulders and a plateau. At higher rates, the initial intercalation voltage of T-Nb$_2$O$_5$ decreases, as expected due to the increased Ohmic contribution; however, not only does the $Q−V$ relationship remain linear but the slope of that line is nearly parallel across more than three orders of magnitude of current. Thus, it seems that, over a very wide

range of current, the amount of charge stored in T-Nb$_2$O$_5$ is determined by the Ohmic potential loss that effectively narrows the potential window for charge storage. Conversely, intercalation into H-Nb$_2$O$_5$ was severely rate limited even at relatively low currents. This evidence suggests a structural (i.e., Li$^+$ transport) limitation such that, even when Ohmic effects are not significant, H-Nb$_2$O$_5$ cannot intercalate lithium rapidly. For example, at C/3 the initial intercalation potential of H-Nb$_2$O$_5$ was approximately 2.1 V, but the shoulder normally at 2.05 V and plateau at 1.67 V were still dampened. In order to test the hypothesis that the electrode/cell resistance is capacity limiting in T-Nb$_2$O$_5$, proof-of-concept 1−2 mg electrodes with additional conductive carbon were constructed and tested under high rate conditions (Figure 7). When the initial
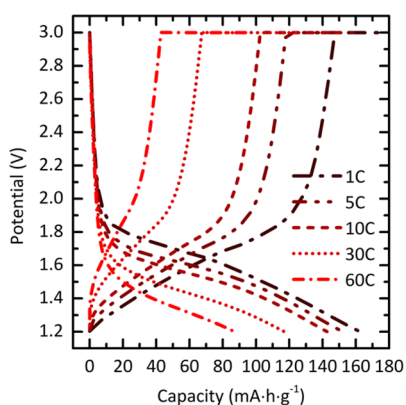

Figure 7. Discharge and charge curves of T-Nb$_2$O$_5$ at current densities ranging from 1C (0.2 A·g^{-1}) to 60C (12.1 A·g^{-1}). A high conductive carbon ratio (2:1) was used to study the discharge profiles at extremely high rates where Ohmic losses are significant. After five cycles, cells were cycled between 3.0 and 1.2 V vs Li$^+$/Li at the rate shown. The charging step is rate limiting for T-Nb$_2$O$_5$; discharge was examined after CCCV charging for uniform comparison.

potential drop is decreased, the trend in linear intercalation with constant slope is found to extend to even higher rates. Capacities of 119 mA·h·g^{-1} and 85 mA·h·g^{-1} were realized in 71 s at 6.05 A·g^{-1} (30C) and 25 s at 12.1 A·g^{-1} (60C), respectively. Again, the discharge capacity appears to be limited by IR drop rather than particle size to at least 60C, despite the fact that it is a bulk material governed by solid-state diffusion and not surface/near-surface reactions. At the high rates and currents required (>10 mA), coin cell resistance, Li$^+$ transport in the electrolyte (particularly between the particles within the electrode film), and lithium anode kinetics all become significant; it is clear that advanced cell design and decreasing the total resistance of the cell/electrode configuration, through e.g., carbon coating or calendaring is important to reach the limits of Nb$_2$O$_5$.

Further characterization of the high rate phases to study the effects of charge-limitation on reversible capacity at different potential windows and rates is presented in the Supporting Information, Figure S5. Upon cycling in a wider potential window (3.0 V−1.0 V), a trade-off is observed between capacity and long-term capacity retention (Figure S5a). Electrochemical cycling without CCCV charging is unable to remove as much lithium from the Nb$_2$O$_5$ framework, resulting in a ca. 25% lower reversible capacity (Figure S5a,b). Even without a potentiostatic charging step, the capacity retention is current-independent and stable throughout 300 cycles (Figure S5b).

4. Lithium Dynamics.
In order to quantify the lithium transport that appears to be inherent to T-Nb$_2$O$_5$, ^{6}Li and ^{7}Li MAS NMR were investigated. Paramagnetic compounds can exhibit lithium resonances shifted over a range of many hundred ppm,[47,48] due to the Fermi contact interaction, yet, despite containing d^1 niobium(IV), Li$_x$Nb$_2$O$_5$ shows ^{7}Li NMR resonances (Figure 8) within a small frequency range for all
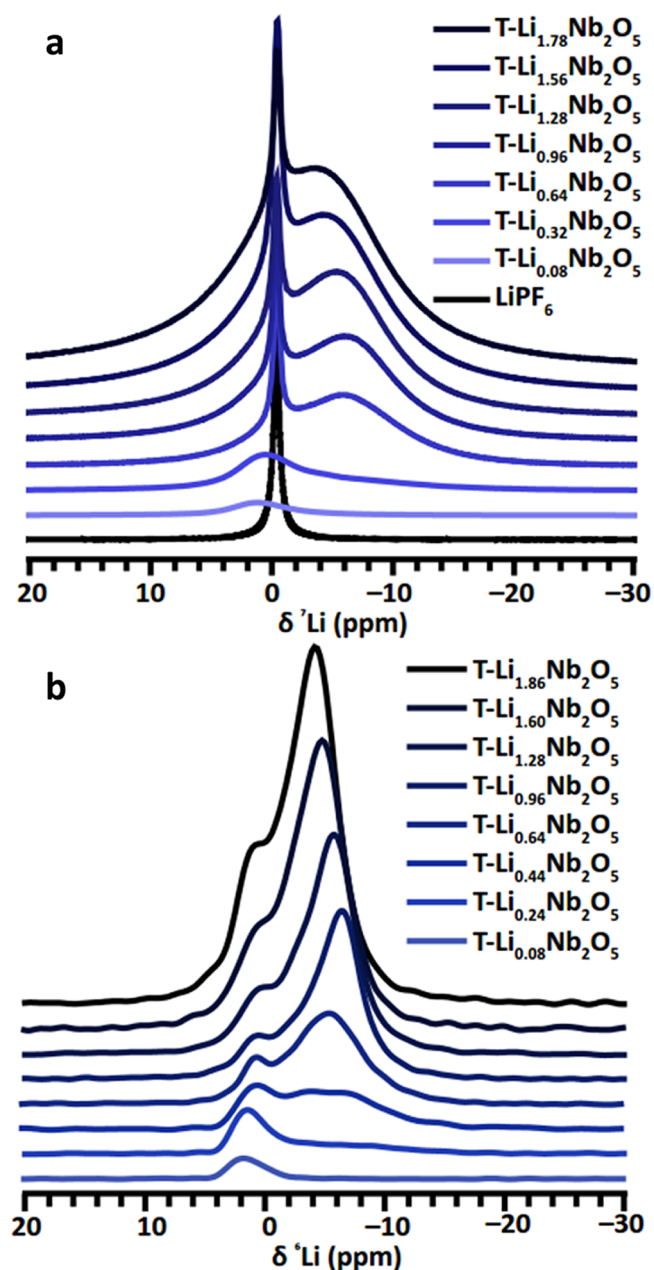

Figure 8. $^{6/7}$Li MAS NMR of Li$_x$Nb$_2$O$_5$. (a) ^{7}Li spectra at 9 kHz MAS and 4.7 T, and (b) ^{6}Li spectra at 9 kHz MAS and 16.4 T. The high-resolution ^{6}Li spectra suggest a distribution of similar lithium local environments.

values of x and longer T_1 relaxation values (∼1s) than expected for ^{7}Li in paramagnetic solids. These values are, however, similar to those observed for Ti^{3+}-containing paramagnetic materials.[49] The spectra shown in Figure 8 and Supporting Information, Figure S6, show the presence of two discrete environments for intercalated lithium. The sharp feature in

Figure 8a comes from residual $LiPF_6$ from the electrolyte, and as seen in Figure S6 disappears entirely upon rinsing with dimethyl carbonate; no observable effect is seen on the peaks from intercalated lithium. The ^6Li spectra at high magnetic field strength (Figure 8b) should, in principle, give the best resolution. This is a result of reduced dipolar broadening from the smaller natural abundance and gyromagnetic ratio of ^6Li vs ^7Li as well as reduced quadrupolar broadening due to both the smaller nuclear quadrupole moment of ^6Li and the higher magnetic field. Despite all this, only a moderate reduction in line width is observed between the ^7Li spectra at a low magnetic field and ^6Li spectra at high magnetic field, which suggests that the peak widths are dominated by the range of shifts caused by a distribution of local environments. Upon discharge, the first lithium ions occupy a site that gives rise to a resonance at 2 ppm. Above $Li_{0.2}Nb_2O_5$, the lithium begin to occupy one or multiple sites with resonances at approximately −5 ppm. As lithiation increases, site(s) with negative shifts are further populated and an increase of shift is observed for all resonances. Given the structural complexity of $T-Nb_2O_5$ with multiple reasonable lithium positions and the lack of crystal structure data for the lithiated compound, there are not presently known crystallographic sites to compare with the local environments derived from NMR.

The collection of high signal-to-noise spectra of ^7Li and natural abundance ^6Li in a matter of minutes was facilitated by the use of thick pellet electrodes. Despite the size (ca. 400−500 mg) and lack of conductive carbon or binder in the pellet design, the structure and electrochemistry upon discharge is identical between the pellets and a conventional film as confirmed by chronopotentiometry (Supplementary Figure S7). Furthermore, lithiated $T-Nb_2O_5$ appears to be quite stable; no changes were observed in the NMR spectra over the course of several months even after intentional exposure to air for a period of 24 h.

Variable-temperature (VT) $^{6,7}Li$ MAS NMR experiments were used to investigate time scales for lithium motion and the electronic structure of lithiated Nb_2O_5. T_1 (spin−lattice) and T_2 (spin−spin) relaxation rates, as well as 1D line shape and 2D spin exchange measurements were recorded over a range of temperatures at low and high magnetic field for selected samples. Figure 9 displays the effect of temperature on the line shape and shift of ^7Li in $Li_xNb_2O_5$ at x = 0.44 and 1.86. Motional line narrowing and loss of rotational sideband intensity is observed which is ascribed to lithium mobility, which averages the chemical shift anisotropy (CSA) and quadrupolar interaction.[50] As the temperature is increased, the lithium resonance at ca. 1 ppm gradually begins to participate in the rapid process at lower frequency.

Above 400 K, the average ^7Li shift moves 1−2 ppm lower in frequency for highly lithiated samples at both 16.4 T (Figure 9) and 4.7 T (not shown). Wagemaker et al.[51] observed this effect in TiO_2 and attributed the increased shielding to a lithium nucleus−electron interaction. Through similar arguments about a small shift range and long T_1s, they concluded that conduction, rather than paramagnetism, was the dominant interaction, accounting for the small observed ^7Li shifts in their system. In addition to electronic changes, the sampling of environments via chemical exchange is temperature-dependent; thus, the nature of the shift may be some combination of conduction and diffusion effects in both the niobium and titanium oxides. We note that an increase in conductivity upon lithiation does suggest delocalization of electrons through the
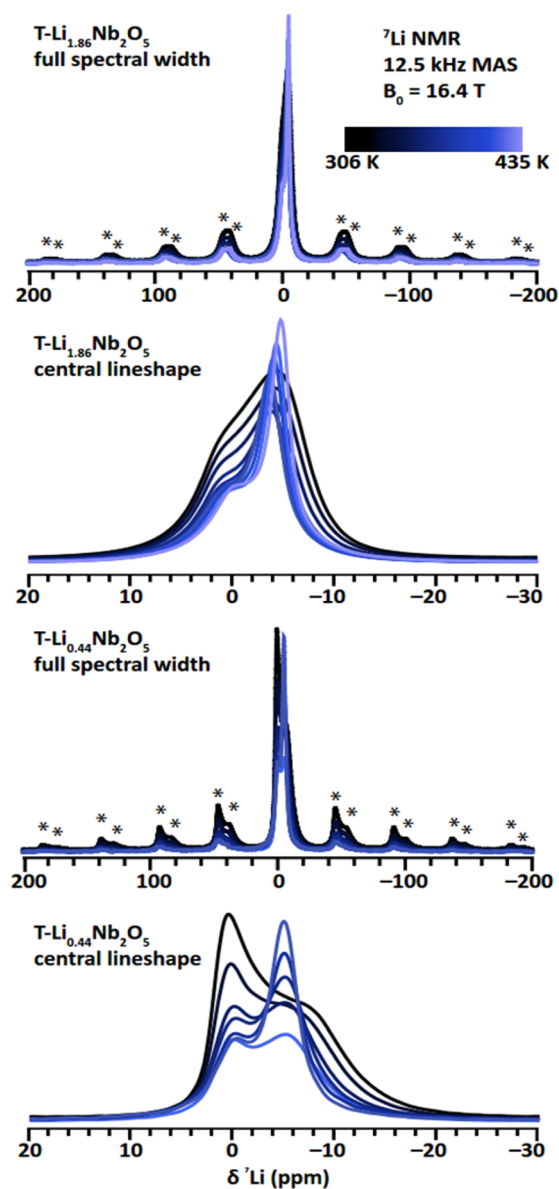

Figure 9. Variable-temperature ^7Li MAS NMR of $Li_xNb_2O_5$ at 12.5 kHz at 16.4 T. The central line shape and rotational sideband manifold (marked by asterisks) are shown for x = 0.44 and x = 1.86 from 306 to 435 K. As the ions become more mobile, sideband intensity decreases and the central line narrows. $T-Li_{0.44}Nb_2O_5$ spectra were normalized to account for T_2 magnetization loss during the echo pulse sequence.

interconnected Nb−O−Nb network in $T-Nb_2O_5$ and offers an explanation for the high-rate and complete lithiation of insulating pellets of $T-Nb_2O_5$ in the absence of conductive additives.

The spin−lattice relaxation time of ^7Li was on the order of 1 s for all lithium concentrations (Figure S8). Spin−spin relaxation was on the order of 1 ms but not strongly temperature dependent in the explored region. The afore-mentioned weak dependence of shift of the resonances on temperature suggests that magnetic effects do not dominate the T_1 changes. Employing the Bloembergen, Purcell, and Pound (BPP)[52] model for random jump diffusion and assuming relaxation dominated by the ^7Li quadrupolar interaction (see Supporting Information for further details)[53,54] at the lower magnetic field strength of 4.7 T, correlation times and trends

for lithium motion were extracted from the variable-temperature T_1 data. Single-exponential fitting of the T_1 relaxation curves was achieved for samples with intermediate to high lithium content; samples below ca. $x = 0.5$ in $Li_xNb_2O_5$ showed a complex multiexponential relaxation curve. The multi-exponential behavior is likely due to the overlapping rigid and mobile lithium resonances, which becomes less significant as the lithium content increases and the mobile lithium sublattice increasingly comprises the overall signal. Strictly, the isotropic BPP model applies to 3D diffusion; however, in the low-temperature regime of the BPP model where T_1 decreases with increasing temperature, 2D diffusion—expected in T-Nb_2O_5—is theoretically[55] and experimentally[56] shown to yield indistinguishable results. Determination of activation energies via the BPP model (Figure 10) yields 98(1), 91(6), 83(5), 68(4), and 58(2) meV for T-$Li_xNb_2O_5$ with $x = 0.64$, 0.96, 1.28, 1.56, and 1.78, respectively.
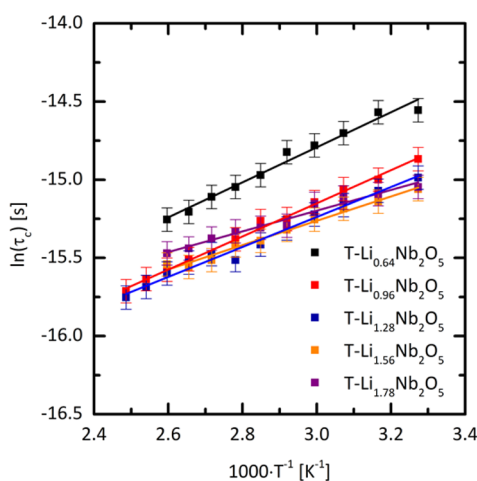

Figure 10. Trend in correlation times derived from the BPP model display Arrhenius behavior. Lithium hopping was found to occur in electrochemically lithiated T-$Li_xNb_2O_5$ with $E_a = 98(1)$, 91(6), 83(5), 68(4), and 58(2) meV for $x = 0.64$, 0.96, 1.28, 1.56, and 1.78, respectively.

Rotor-synchronized MAS two-dimensional exchange spectroscopy (EXSY) data were also recorded for ^7Li. These experiments have proven to be a useful tool to probe dynamics on a microsecond to millisecond time scale.[57,58] Figure 11 shows the ^7Li exchange spectra of T-$Li_{0.44}Nb_2O_5$ as a function of mixing time at 16.4 T and 12.5 kHz MAS. The presence of a narrow diagonal in Figure 11a provides direct evidence that the peaks in the 1D spectra are not true singular broad components but comprised of distributions of individual lithium environments. Exchange between these local environments occurs when the spins are allowed to interact for 1 ms or longer. On the other hand, the intensity pattern and cross sections through the spectra indicate that exchange on this time scale is not occurring between the ca. 1 ppm resonance and the lower frequency distribution of sites. Thus, the lithium in T-Nb_2O_5 can be more precisely described as two reservoirs: a weakly bound distribution of sites with resonances centered around −5 ppm and a more rigid lithium sublattice with resonances at 1 ppm. Note that spin exchange in solids can occur through chemical exchange or dipole-mediated spin interactions; variable-temperature EXSY spectra showed a strong temperature dependence, which is indicative that chemical exchange

dominates spin diffusion in these spectra. Qualitatively similar results were obtained from EXSY measurements at higher lithium contents (Supplementary Figure S9); the increased off-diagonal intensity observed at 100 μs in $Li_{1.28}Nb_2O_5$ and $Li_{1.86}Nb_2O_5$ indicates that exchange occurs on a shorter time scale at higher lithium concentrations.

5. Structure−Property Relationships. In light of the observations on micrometer-sized TT-, T-, B-, and H-Nb_2O_5, their respective electrochemical performance appears to be strongly dictated by inherent crystallographic properties. All Nb_2O_5 polymorphs presented herein may be viewed as being derived from layered structures; however the nature of these layers differs in all cases and all are distinct from the O3 and P2 type[59] layered structures found in $LiCoO_2$ and $Na_{0.7}CoO_2$, respectively. Herein, we describe T-Nb_2O_5 as a "room-and-pillar" framework with alternating layers (along c) of bridging oxygen "pillars" and O−Nb polygons; the interlayer distance is 3.93 Å. Unlike classical layered structures with structural lithium slabs, the room-and-pillar framework is self-supporting and allows lithium to act as a true guest atom over the whole range of $0 \leq x \leq 2$ in $Li_xNb_2O_5$. *In situ* laboratory XRD from several groups[26,33] has suggested that intercalation into T-Nb_2O_5 is accompanied by an expansion of the layers in a solid-solution reaction. B-Nb_2O_5 is structurally similar to $TiO_2(B)$ with bilayers of edge-sharing octahedra; the interlayer distance is 3.51 Å. The layers of H-Nb_2O_5 comprise ReO_3-type blocks of dimension $(3{\times}4)_1$ and $(3{\times}5)_\infty$ NbO_6 octahedra, exhibiting crystallographic shear; the layers are offset from one another by $1/2$ b with an interlayer distance of 3.83 Å. Given the complexity of these layered oxides and the distortion of the individual polyhedra due to the second-order Jahn−Teller effect of d^0 Nb^{5+}, the sites and diffusion pathways for lithiation may not be immediately discernible. In order to overcome this challenge, we applied the bond valence sum (BVS) mapping method to Nb_2O_5 and related structures (Figure 12). The BVS method is a commonly employed tool to validate trial structures during crystal structure solution and refinement; however, it may be extended to help predict theoretical sites and diffusion pathways through BVS mapping. This method has proven to be an accurate and useful tool for the qualitative evaluation of atomic sites and diffusion pathways in a range of materials.[60] It should be especially relevant where solid-solution or only minor rearrangement occur during lithiation; the use of this approach to study two-phase reactions should be treated with care as diffusion through the structure and lithium positions within the structure are not representative of a reaction across a boundary to a distinct phase. In this study, the program 3DBVSMapper[61] was used to calculate the BVS of a theoretical lithium at each position on a fine grid over a unit cell. Starting with T-Nb_2O_5 (Figure 12a,b), one can visualize the nearly degenerate 2D diffusion pathways throughout the structure as represented by the continuous 2 eV isosurface. The isosurface energy is a relative value and does not correspond trivially to a measurable physical quantity; it is most instructive to use an energy corresponding to the onset of sites/connected pathways to see those relatively low in energy.[60,61] The high degree of favorable sites on interconnected pathways without obvious minima to trap lithium offers some qualitative insight into the fast kinetics of the system. The BVS map of H-Nb_2O_5 (Figure 12c,d) reveals that within the ReO_3 (Figure 12e)-type blocks there are large spaces where lithium may reside; however, these large vacancies with 12 nearest-neighbor oxygens are too big for lithium, which is likely to find an off-
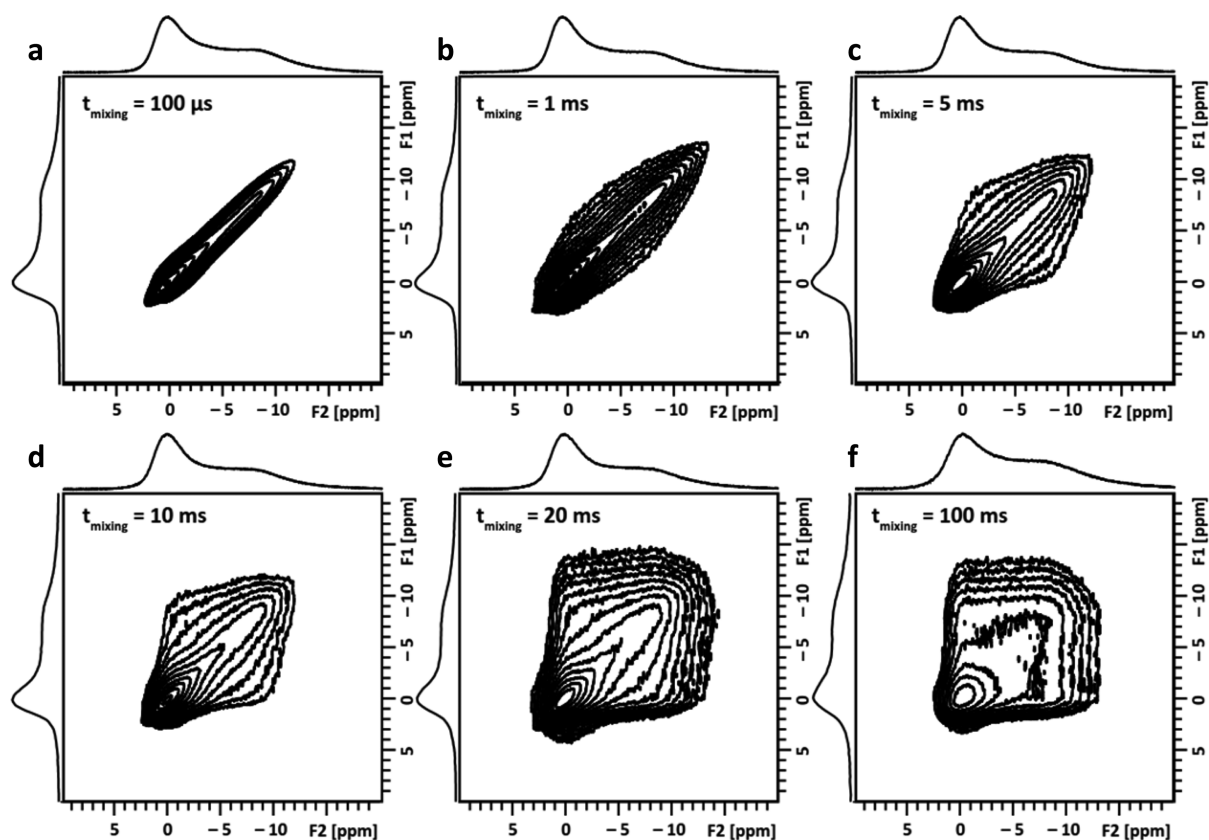
Figure 11. ^{7}Li EXSY spectra of T-Li$_{0.44}$Nb$_2$O$_5$ with mixing periods of (a) 100 μs, (b) 1 ms, (c) 5 ms, (d) 10 ms, (e) 20 ms, and (f) 100 ms. Spectra were collected at 12.5 kHz MAS, 306 K, and 16.4 T.
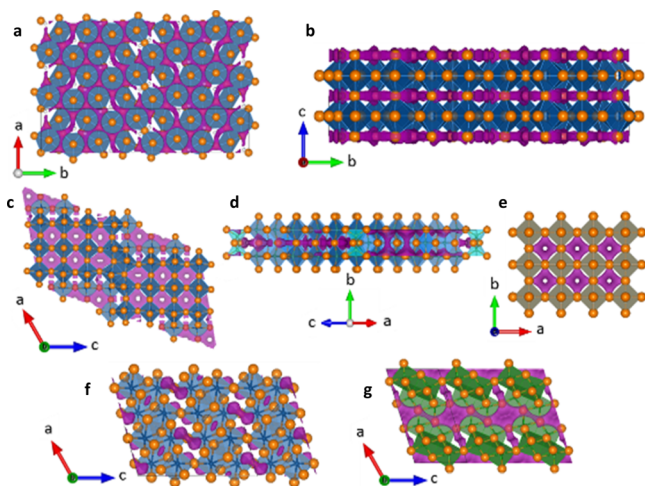

Figure 12. Bond valence sum maps of (a,b) T-Nb$_2$O$_5$, (c,d) H-Nb$_2$O$_5$, (e) ReO$_3$, (f) B-Nb$_2$O$_5$, (g) TiO$_2$(B). Bond valence energy level calculations were performed for a theoretical grid of Li$^+$, and 2.0 eV isosurfaces are shown in purple.

center local minimum. In a true ReO$_3$-type structure such as NbO$_2$F, topotactic lithiation would theoretically lead to an ABX$_3$ perovskite but the size-mismatch instability instead leads to tilting of the BX$_3$ octahedra to reduce the size of the A site, and a distortion toward the LiNbO$_3$ structure.[62] The crystallographic shear in H-Nb$_2$O$_5$ and related compounds such as TiNb$_2$O$_7$[63,64] precludes these tilting and distortion modes that are common in perovskites, which will have implications for Li$^+$ mobility within the perovskite blocks. The

BVS map of H-Nb$_2$O$_5$ indicates, via breaks in the isosurface, that there is a relatively high energy barrier to diffusion between the 3×4 and 3×5 blocks. The abundance of lithium sites, which have been observed via neutron diffraction for H-Li$_{12/7}$Nb$_2$O$_5$,[65] but local minima and poor connectivity of diffusion pathways helps to explain the high capacity but poor rate performance of H-Nb$_2$O$_5$. On the other hand, the 2 eV isosurface for B-Nb$_2$O$_5$ (Figure 12f) shows only discrete sites between the layers. Given the structural similarity to TiO$_2$(B) (Figure 12g), one might expect significant and perhaps high-rate lithiation into B-Nb$_2$O$_5$; however, the slightly smaller interlayer spacing (3.51 vs 3.66 Å) and higher oxidation state (Nb^{5+} vs Ti^{4+}) apparently preclude facile lithiation.

■ DISCUSSION

In stark contrast to the well-known positive effects of nanoscaling in Li$_4$Ti$_5$O$_{12}$,[66,67] LiCoO$_2$,[68] LiFePO$_4$,[69,70] MnO$_2$,[71,72] and polymorphs of TiO$_2$ (e.g., anatase, rutile, TiO$_2$(B), brookite),[2] both the total charge storage capacity and the rate performance of thick electrodes of bulk TT- and particularly T-Nb$_2$O$_5$ are comparable to the best nano-structured Nb$_2$O$_5$ particle geometries.[18,20,23] It is important to stress that care must be taken when comparing high-rate electrochemical data in the literature; in particular, cyclic voltammetric (CV) and chronopotentiometric (i.e., galvano-static) methods are not necessarily directly comparable. For Nb$_2$O$_5$ with a theoretical capacity of 201.7 mA·h·g^{-1}, a rate of 1C corresponds to 201.7 mA·g^{-1} and a time of 1 h for one electron/one lithium discharge. The corresponding experiment via CV is conducted at a sweep rate determined by the potential window divided by the desired discharge time (e.g., 3600 s).

Thus, a change in the potential window will translate to a change in the sweep rate without affecting the C rate. More significantly, the discharge time from CV will always be longer than the time for a high-rate galvanostatic experiment that does not reach theoretical capacity (and fast discharge rarely ever reaches theoretical capacity). A sweep of 1200 mV at 20 mV·s^{-1} requires 60 s and is therefore called 60C while T-Nb$_2$O$_5$ reaches only *circa* half of theoretical capacity at this rate and thus requires only a 30 s galvanostatic discharge. The applied galvanostatic current at 60C for T-Nb$_2$O$_5$ is by definition 12.1 A·g^{-1} while the average current in a CV experiment would be scaled by the percent of theoretical capacity attained (i.e., 6.05 A·g^{-1} in this example). Since ohmic (IR) losses become significant at high currents, galvanostatic cycling further suffers as the enforcement of a single initial current means the full IR drop is realized at the start of discharge. For reference, the curves denoted 30C and 60C in Figure 7 were acquired in 71 and 25 s, respectively, rather than 120 and 60 s if recorded via CV. This difference is significant for high-rate materials and high-power applications.

The activation barriers in T-Li$_x$Nb$_2$O$_5$ at 98(1)−58(2) meV are significantly lower than those found in other lithium-ion battery materials: Li$_{0.7}$TiS$_2$ at 370−410 meV,[56] Li$_6$Ti$_5$O$_{12}$ at 430 meV,[73] Li$_4$Ti$_5$O$_{12}$ at 760 meV,[73] Li$_{0.74}$TiO$_2$ at 370 meV,[49] and LiFePO$_4$ at 270−500 meV.[74] The dynamics of T-Li$_x$Nb$_2$O$_5$ are more similar to several recently reported Li-rich solid electrolyte materials;[75,76] Li$_{10}$GeP$_2$S$_{12}$, Li$_7$GePS$_8$, and Li$_{11}$Si$_2$PS$_{12}$ show activation barriers for lithium motion of 200−250 meV. NMR relaxometry is a microscopic probe of lithium diffusion and it is known that, in certain cases, the thermally activated process was not one of bulk diffusion but, for example, local librational motion of protons[77] or restricted lithium hopping in a system where diffusion is controlled by phase or grain boundaries.[51] From the structural arguments presented above, the large particles, degenerate atomic diffusion pathways, and apparent lack of phase transition in T-Nb$_2$O$_5$ suggest that, analogous to the layered compound Li$_{0.7}$TiS$_2$,[56] the microscopic processes translate to the macroscale.

The high rate capability observed for micrometer-sized particles of bronze-phase Nb$_2$O$_5$ is somewhat remarkable. To place context for this result, it is useful to compare to TiO$_2$ more explicitly as titanium(IV) oxide is chemically similar to niobium(V) oxide in that both are insulators with a d^0 cation with similar ionic radii and several known polymorphs. The maximum capacity of all aforementioned TiO$_2$ polymorphs is higher for nanoparticles than the bulk phase, e.g. in anatase TiO$_2$, a careful study demonstrated that full lithiation to LiTiO$_2$ occurred only for particles <7−15 nm while bulk anatase reached a maximum lithium content of Li$_{0.5-0.6}$TiO$_2$ and the term "bulk" was applied to anything over ca. 120 nm.[78] In terms of rate, it was shown that full capacity at 5C to 10C rates required sub-10 nm particles. Thus, it is generally accepted that both the maximum capacity and rate performance are size-dependent properties in anatase TiO$_2$. A first-principles thermodynamic and kinetic study[79] by the Van der Ven group showed that, as TiO$_2$ is lithiated and Ti^{4+} is reduced to Ti^{3+}, the distortions in octahedral titanium sites are removed, which causes the minimal energy migration paths to increase from 0.50 to 0.78 eV to 1.37 eV for dilute Li$_x$TiO$_2$, Li$_{0.5}$TiO$_2$ and LiTiO$_2$, respectively. While polyhedra in niobium(V) and titanium(IV) oxides experience similar second-order Jahn−Teller distortions,[80] the relaxation of these distortions from niobium(V) to niobium(IV) in the bronze-phase Nb$_2$O$_5$

structure does not cause the same clamping of diffusion paths. Thus, the impetus to nanosize TiO$_2$ to suppress phase transitions and increase lattice flexibility is not as applicable to Nb$_2$O$_5$. The results presented here suggest that optimal performance of Nb$_2$O$_5$ is observed even on the scale of micrometers rather than only at a few nanometers. Furthermore, despite the insulating nature of Nb$_2$O$_5$, the performance herein is comparable to nanocrystalline Nb$_2$O$_5$/carbon nanocomposites with graphene,[29,30] carbon nanotubes,[28] carbide-derived carbon,[31] and carbon core−shell nanocrystals,[32] which, along with the immediate color change, suggests that Nb$_2$O$_5$ must undergo significant conductivity changes even at low lithium content as electrons are introduced into the transition metal d-orbitals. This rate behavior for solid-state-derived Nb$_2$O$_5$ is observed in the absence of thin electrodes, lithium perchlorate salts, and carbon counter electrodes that are frequently reported to improve Nb$_2$O$_5$ rate capability.[26,27]

■ CONCLUSIONS

Via solid-state synthesis and electrochemical characterization, we have demonstrated that the complex oxide structure of T-Nb$_2$O$_5$ facilitates high-rate lithium intercalation into large particles on par with the best nanostructured electrodes. Lithium dynamics were investigated with variable-temperature NMR relaxation and exchange measurements on electrochemically lithiated T-Nb$_2$O$_5$, which revealed an activation barrier for microscopic lithium diffusion on the order of a few $k_B T$ (ca. 60−100 meV). Intercalation of lithium into the room-and-pillar layered structure of T-Nb$_2$O$_5$ results in high ionic mobility and minimal strain, which negates the usual requirement of short diffusion pathways and phase transition-suppressing nanoparticles for rapid discharge. Temperature-dependent NMR shifts at high lithium content suggest delocalized conduction electrons and clarify the electronic aspect of the observed high-rate performance in this originally wide-bandgap oxide. Atomic origins of the vast differences in electrochemical behavior among Nb$_2$O$_5$ polymorphs were elucidated. The bulk properties of high-rate TT- and T-Nb$_2$O$_5$, low-capacity B-Nb$_2$O$_5$, and high-capacity but low-rate H-Nb$_2$O$_5$ can be understood in terms of their structure and relationships to other compounds aided by lithium bond valence sum maps. The volumetric power and energy density, safety, stability, and ease of synthesis make Nb$_2$O$_5$ an interesting candidate for energy storage applications demanding combined high rate and high capacity in a small cell. We believe the structural principles and techniques presented here will aid the exploration of materials space for future high-rate electrode materials, especially for complex structures that may offer unique advantages with minimal synthetic or post-synthetic processing. Forthcoming work will examine the structural transitions, lithium dynamics, and lithium sites in H-Nb$_2$O$_5$, which are beyond the scope of this study.

■ ASSOCIATED CONTENT

Ⓢ Supporting Information

The Supporting Information is available free of charge on the ACS Publications website at DOI: 10.1021/jacs.6b04345.

> Rietveld refinements, additional SEM micrographs, electrochemical cycling data, ^{7}Li MAS NMR spectral deconvolutions, details of the data fitting and temperature calibration for VT NMR, chronopotentiometric

comparison of film and pellet electrodes, and additional data from relaxometry and exchange spectroscopy measurements (PDF)

AUTHOR INFORMATION

Corresponding Author

*cpg27@cam.ac.uk

Notes

The authors declare no competing financial interest.
Data supporting this work are available from www.repository.cam.ac.uk.

REFERENCES

(1) Conway, B. E. *Electrochemical Supercapacitors: Scientific Fundamentals and Technological Applications*; Springer: New York, 1999.

(2) Dylla, A. G.; Henkelman, G.; Stevenson, K. J. *Acc. Chem. Res.* **2013**, *46*, 1104−1112.

(3) Wagemaker, M.; Mulder, F. M. *Acc. Chem. Res.* **2013**, *46*, 1206−1215.

(4) Buzea, C.; Pacheco, I. I.; Robbie, K. *Biointerphases* **2007**, *2*, 17−71.

(5) Palacin, M. R.; Simon, P.; Tarascon, J. M. *Acta Chim. Slov.* **2016**, *63*, 2314.

(6) Reddy, M. A.; Varadaraju, U. V. *J. Phys. Chem. C* **2011**, *115*, 25121−25124.

(7) Han, J.-T.; Liu, D.-Q.; Song, S.-H.; Kim, Y.; Goodenough, J. B. *Chem. Mater.* **2009**, *21*, 4753−4755.

(8) Han, J.-T.; Goodenough, J. B. *Chem. Mater.* **2011**, *23*, 3404−3407.

(9) Wen, C. J.; Boukamp, B. A.; Huggins, R. A.; Weppner, W. *J. Electrochem. Soc.* **1979**, *126*, 2258−2266.

(10) Schäfer, H.; Gruehn, R.; Schulte, F. *Angew. Chem., Int. Ed. Engl.* **1966**, *5*, 40−52.

(11) Frevel, L. K.; Rinn, H. W. *Anal. Chem.* **1955**, *27*, 1329−1330.

(12) Weissman, J. G.; Ko, E. I.; Wynblatt, P.; Howe, J. M. *Chem. Mater.* **1989**, *1*, 187−193.

(13) Ko, E. I.; Weissman, J. G. *Catal. Today* **1990**, *8*, 27−36.

(14) Kato, K.; Tamura, S. *Acta Crystallogr., Sect. B: Struct. Crystallogr. Cryst. Chem.* **1975**, *31*, 673−677.

(15) Laves, F.; Petter, W.; Wulf, H. *Naturwissenschaften* **1964**, *51*, 633−634.

(16) Kato, K. *Acta Crystallogr., Sect. B: Struct. Crystallogr. Cryst. Chem.* **1976**, *32*, 764−767.

(17) Anderson, J. S.; Tilley, R. J. D. In *Surface and Defect Properties of Solids*; The Chemical Society: London, 1974; Vol. 3, pp 1−56.

(18) Wei, M.; Wei, K.; Ichihara, M.; Zhou, H. *Electrochem. Commun.* **2008**, *10*, 980−983.

(19) Viet, A. L.; Reddy, M. V.; Jose, R.; Chowdari, B. V. R.; Ramakrishna, S. *J. Phys. Chem. C* **2010**, *114*, 664−671.

(20) Liu, M.; Yan, C.; Zhang, Y. *Sci. Rep.* **2015**, *5*, 8326.

(21) Luo, H.; Wei, M.; Wei, K. *Mater. Chem. Phys.* **2010**, *120*, 6−9.

(22) Brezesinski, K.; Wang, J.; Haetge, J.; Reitz, C.; Steinmueller, S. O.; Tolbert, S. H.; Dunn, B. *J. Am. Chem. Soc.* **2010**, *132*, 6982−6990.

(23) Kong, L.; Zhang, C.; Wang, J.; Long, D.; Qiao, W.; Ling, L. *Mater. Chem. Phys.* **2015**, *149−150*, 495−504.

(24) Lim, E.; Kim, H.; Jo, C.; Chun, J.; Ku, K.; Kim, S.; Lee, H. I.; Nam, I.-S.; Yoon, S.; Kang, K.; Lee, J. *ACS Nano* **2014**, *8*, 8968−8978.

(25) Kim, J. W.; Augustyn, V.; Dunn, B. *Adv. Energy Mater.* **2012**, *2*, 141−148.

(26) Come, J.; Augustyn, V.; Kim, J. W.; Rozier, P.; Taberna, P.-L.; Gogotsi, P.; Long, J. W.; Dunn, B.; Simon, P. *J. Electrochem. Soc.* **2014**, *161*, A718−A725.

(27) Augustyn, V.; Come, J.; Lowe, M. A.; Kim, J. W.; Taberna, P.-L.; Tolbert, S. H.; Abruña, H. D.; Simon, P.; Dunn, B. *Nat. Mater.* **2013**, *12*, 518−522.

(28) Wang, X.; Li, G.; Chen, Z.; Augustyn, V.; Ma, X.; Wang, G.; Dunn, B.; Lu, Y. *Adv. Energy Mater.* **2011**, *1*, 1089−1093.

(29) Long, D.; Kong, L.; Zhang, C.; Zhang, S.; Wang, J.; Cai, R.; Lv, C.; Qiao, W. M.; Ling, L. *J. Mater. Chem. A* **2014**, *2*, 17962−17970.

(30) Arunkumar, P.; Ashish, A. G.; Babu, B.; Sarang, S.; Suresh, A.; Sharma, C. H.; Thalakulam, M.; Shaijumon, M. M. *RSC Adv.* **2015**, *5*, 59997−60004.

(31) Zhang, C.; Maloney, R.; Lukatskaya, M. R.; Beidaghi, M.; Dyatkin, B.; Perre, E.; Long, D.; Qiao, W.; Dunn, B.; Gogotsi, Y. *J. Power Sources* **2015**, *274*, 121−129.

(32) Lim, E.; Jo, C.; Kim, H.; Kim, M.-H.; Mun, Y.; Chun, J.; Ye, Y.; Hwang, J.; Ha, K.-S.; Roh, K. C.; Kang, K.; Yoon, S.; Lee, J. *ACS Nano* **2015**, *9*, 7497−7505.

(33) Kumagai, N.; Koishikawa, Y.; Komaba, S.; Koshiba, N. *J. Electrochem. Soc.* **1999**, *146*, 3203−3210.

(34) Kodama, R.; Terada, Y.; Nakai, I.; Komaba, S.; Kumagai, N. *J. Electrochem. Soc.* **2006**, *153*, 583−588.

(35) A. C, Larson; Von Dreele, R. B. *General Structure Analysis System (GSAS)*, LAUR 86-748; Los Alamos National Laboratory: Los Alamos, NM, 2000.

(36) Toby, B. H.; Von Dreele, R. B. *J. Appl. Crystallogr.* **2013**, *46*, 544−549.

(37) Toby, B. H. *J. Appl. Crystallogr.* **2005**, *38*, 1040−1041.

(38) Momma, K.; Izumi, F. *J. Appl. Crystallogr.* **2011**, *44*, 1272−1276.

(39) Bielecki, A.; Burum, D. P. *J. Magn. Reson., Ser. A* **1995**, *116*, 215−220.

(40) Maruyama, T.; Arai, S. *Appl. Phys. Lett.* **1993**, *63*, 869−870.

(41) Titanium Oxide (TiO2) Nanoparticles/Nanopowder (TiO2, Anatase, 99.5% 5nm) http://www.us-nano.com/inc/sdetail/20769 (accessed Dec 8, 2015).

(42) Meyer, G.; Hoppe, R. *J. Less-Common Met.* **1976**, *46*, 55−65.

(43) Kumada, N.; Muramatu, S.; Muto, F.; Kinomura, N.; Kikkawa, S.; Koizumi, M. *J. Solid State Chem.* **1988**, *73*, 33−39.

(44) Reddy, M. V.; Jose, R.; Le Viet, A.; Ozoemena, K. I.; Chowdari, B. V. R.; Ramakrishna, S. *Electrochim. Acta* **2014**, *128*, 198−202.

(45) Saito, K.; Kudo, A. *Bull. Chem. Soc. Jpn.* **2009**, *82*, 1030−1034.

(46) Rauda, I. E.; Augustyn, V.; Dunn, B.; Tolbert, S. H. *Acc. Chem. Res.* **2013**, *46*, 1113−1124.

(47) Middlemiss, D. S.; Ilott, A. J.; Clément, R. J.; Strobridge, F. C.; Grey, C. P. *Chem. Mater.* **2013**, *25*, 1723−1734.

(48) Strobridge, F. C.; Clément, R. J.; Leskes, M.; Middlemiss, D. S.; Borkiewicz, O. J.; Wiaderek, K. M.; Chapman, K. W.; Chupas, P. J.; Grey, C. P. *Chem. Mater.* **2014**, *26*, 6193−6205.

(49) Bottke, P.; Ren, Y.; Hanzu, I.; Bruce, P. G.; Wilkening, M. *Phys. Chem. Chem. Phys.* **2014**, *16*, 1894−1901.

(50) Schurko, R. W.; Wi, S.; Frydman, L. *J. Phys. Chem. A* **2002**, *106*, 51−62.

(51) Wagemaker, M.; van de Krol, R.; Kentgens, A. P. M.; van Well, A. A.; Mulder, F. M. *J. Am. Chem. Soc.* **2001**, *123*, 11454−11461.

(52) Bloembergen, N.; Purcell, E. M.; Pound, R. V. *Phys. Rev.* **1948**, *73* (7), 679−712.

(53) Abragam, A. *Principles of Nuclear Magnetism*; International Series of Monographs on Physics; Oxford Science Publications: Oxford, 1961.

(54) Steigel, A.; Spiess, H. W. *Dynamic NMR Spectroscopy*; NMR Basic Principles and Progress; Springer: Berlin, 1978.

(55) *Diffusion in Condensed Matter*; Heitjans, P., Kärger, J., Eds.; Springer: Berlin, 2005.

(56) Wilkening, M.; Küchler, W.; Heitjans, P. *Phys. Rev. Lett.* **2006**, *97*, 65901.

(57) Xu, Z.; Stebbins, J. F. *Science* **1995**, *270*, 1332−1334.

(58) Davis, L. J. M.; Heinmaa, I.; Goward, G. R. *Chem. Mater.* **2010**, *22*, 769−775.

(59) Yabuuchi, N.; Kawamoto, Y.; Hara, R.; Ishigaki, T.; Hoshikawa, A.; Yonemura, M.; Kamiyama, T.; Komaba, S. *Inorg. Chem.* **2013**, *52*, 9131−9142.

(60) Avdeev, M.; Sale, M.; Adams, S.; Rao, R. P. *Solid State Ionics* **2012**, *225*, 43−46.

(61) Sale, M.; Avdeev, M. *J. Appl. Crystallogr.* **2012**, *45*, 1054−1056.

(62) Bohnke, C.; Bohnke, O.; Fourquet, J. L. *Mol. Cryst. Liq. Cryst. Sci. Technol., Sect. A* **1998**, *311*, 23−29.

(63) Lu, X.; Jian, Z.; Fang, Z.; Gu, L.; Hu, Y.-S.; Chen, W.; Wang, Z.; Chen, L. *Energy Environ. Sci.* **2011**, *4*, 2638−2644.

(64) Dreele, R. B. V.; Cheetham, A. K. *Proc. R. Soc. London, Ser. A* **1974**, *338*, 311−326.

(65) Catti, M.; Ghaani, M. R. *Phys. Chem. Chem. Phys.* **2014**, *16*, 1385−1392.

(66) Borghols, W. J. H.; Wagemaker, M.; Lafont, U.; Kelder, E. M.; Mulder, F. M. *J. Am. Chem. Soc.* **2009**, *131*, 17786−17792.

(67) Liu, W.; Zhang, J.; Wang, Q.; Xie, X.; Lou, Y.; Xia, B. *Ionics* **2014**, *20*, 1553−1560.

(68) Okubo, M.; Hosono, E.; Kim, J.; Enomoto, M.; Kojima, N.; Kudo, T.; Zhou, H.; Honma, I. *J. Am. Chem. Soc.* **2007**, *129*, 7444−7452.

(69) Delacourt, C.; Poizot, P.; Levasseur, S.; Masquelier, C. *Electrochem. Solid-State Lett.* **2006**, *9*, 352−355.

(70) Huang, H.; Yin, S.-C.; Nazar, L. F. *Electrochem. Solid-State Lett.* **2001**, *4*, 170−172.

(71) Devaraj, S.; Munichandraiah, N. *J. Phys. Chem. C* **2008**, *112*, 4406−4417.

(72) Ren, Y.; Armstrong, A. R.; Jiao, F.; Bruce, P. G. *J. Am. Chem. Soc.* **2010**, *132*, 996−1004.

(73) Wilkening, M.; Iwaniak, W.; Heine, J.; Epp, V.; Kleinert, A.; Behrens, M.; Nuspl, G.; Bensch, W.; Heitjans, P. *Phys. Chem. Chem. Phys.* **2007**, *9*, 6199−6202.

(74) Liu, Z.; Huang, X. *Solid State Ionics* **2010**, *181*, 907−913.

(75) Kuhn, A.; Gerbig, O.; Zhu, C.; Falkenberg, F.; Maier, J.; Lotsch, B. V. *Phys. Chem. Chem. Phys.* **2014**, *16*, 14669−14674.

(76) Kuhn, A.; Duppel, V.; Lotsch, B. V. *Energy Environ. Sci.* **2013**, *6*, 3548.

(77) Kim, G.; Blanc, F.; Hu, Y.-Y.; Grey, C. P. *J. Phys. Chem. C* **2013**, *117*, 6504−6515.

(78) Wagemaker, M.; Borghols, W. J. H.; Mulder, F. M. *J. Am. Chem. Soc.* **2007**, *129*, 4323−4327.

(79) Belak, A. A.; Wang, Y.; Van der Ven, A. *Chem. Mater.* **2012**, *24*, 2894−2898.

(80) Kunz, M.; Brown, I. D. *J. Solid State Chem.* **1995**, *115*, 395−406.